JGR Solid Earth

RESEARCH ARTICLE
10.1029/2021JB022489

This article is a companion to Tregoning et al. (2022), https://doi.org/10.1029/2021JB022412.

Key Points:

- Mass anomalies are derived from GRACE inter-satellite range acceleration observations
- High levels of high-frequency noise present in the Level-1B range acceleration observation can be mitigated with appropriate pre-processing
- Our solutions on major ice sheets, the Amazon basin and over oceans derived with the range acceleration agree with other processing centers

Supporting Information:

Supporting Information may be found in the online version of this article.

Correspondence to:

S. Allgeyer,
Sebastien.Allgeyer@anu.edu.au

Citation:

Allgeyer, S., Tregoning, P., McQueen, H., McClusky, S. C., Potter, E.-K., Pfeffer, J., et al. (2022). ANU GRACE Data analysis: Orbit modeling, regularization and inter-satellite range acceleration observations. *Journal of Geophysical Research: Solid Earth*, *127*, e2021JB022489. https://doi.org/10.1029/2021JB022489

Received 24 MAY 2021
Accepted 8 JAN 2022

ANU GRACE Data Analysis: Orbit Modeling, Regularization and Inter-satellite Range Acceleration Observations

S. Allgeyer[1], P. Tregoning[1], H. McQueen[1], S. C. McClusky[1], E.-K. Potter[1,2], J. Pfeffer[1,3], R. McGirr[1], A. P. Purcell[1], T. A. Herring[4], and J.-P. Montillet[1,5]

[1]Research School of Earth Sciences, Australian National University, Canberra, ACT, Australia, [2]Now at Canberra College, Phillip, ACT, Australia, [3]Now at Magellium, Toulouse, France, [4]Department of Earth, Atmospheric and Planetary Sciences, Massachusetts Institute of Technology, Cambridge, MA, USA, [5]Now at Physikalische-Meteorologische Observatorium Davos (PMOD), World Radiation Center, Davos, Switzerland

Abstract Several different basis functions have been used to represent the Earth's gravity field in order to generate estimates of mass variations on Earth from the analysis of data of the Gravity Recovery and Climate Experiment (GRACE) and its successor GRACE Follow-On missions, including spherical harmonics, mass concentration elements (mascons) and slepian functions. Each approach depends inherently upon accurate modeling of the orbits of the pair of satellites as they revolve around the Earth, so that the observations of inter-satellite changes in range (or, more specifically, range rate) can be exploited to identify mass variations. We have developed software using a classical orbit modeling approach, mascons and 24-hr orbit integration, to estimate simultaneously corrections to orbital parameters and the temporal gravity field from GRACE data. Rather than using the range rate, we use the range acceleration as the inter-satellite observable as it aids in localizing the mass variations. Level-1 B range acceleration observations contain high levels of high-frequency noise that inhibits their usefulness for this purpose. Instead, we generate range acceleration observations by numerical differentiation of the Level-1B range rate prefit residuals. Simulations show that the gravity signal is not attenuated in this process. Our monthly estimates of mass anomalies from GRACE data (2003–2016) agree well with previous studies, both spatially and temporally. When converted to spherical harmonics our time series of $C_{2,0}$, derived from GRACE data alone, are close to the independent estimates from satellite laser ranging, but the overall solution is improved by substituting the SLR $C_{2,0}$.

Plain Language Summary The Gravity Recovery and Climate Experiment (GRACE) space gravity mission consists of a pair of identical twin satellites one following the other and separated by about 200 km. The distance between the satellites is altered by mass distribution on Earth. While all published temporal gravity field models are estimated from the rate of change of the inter-satellite distances (known as range rate), this study uses the relative acceleration (known as range acceleration) between the satellites as the observation to determine the distribution of mass on Earth. The methodology we developed has multiple advantages with respect to solutions derived using the range rate. Mass changes on Earth are located spatially with greater accuracy and have a better resolution of the long wavelength gravity field.

1. Introduction

The Gravity Recovery and Climate Experiment (GRACE) space gravity mission (Tapley et al., 2004) operated from 2002 until it was decommissioned in 2017. Data from the mission have had major impacts in the fields of hydrology (e.g., Leblanc et al., 2009; Lo et al., 2010; Rodell et al., 2018), cryospheric science (e.g., Luthcke et al., 2013; Velicogna, 2006), oceanography (e.g., Boening et al., 2012; Chambers, 2006) and glacial isostasy (e.g., Martín-Español et al., 2016; Riva et al., 2009). Small changes in the strength of the Earth's gravity field caused by the redistribution of mass on the Earth cause subtle changes in the range between the satellites. This is the fundamental observation that made the GRACE mission unique.

A number of different mathematical approaches have been used to parameterize the Earth's gravity field and the convergence of the inversions of the data. Solving for coefficients of spherical harmonic models has been the most common approach used since the start of the GRACE mission (e.g., Lemoine et al., 2007; Tapley et al., 2004). A common characteristic of the estimated temporal gravity fields is a north-south striped error pattern, in part related to the high correlations between even and odd order coefficients (Swenson & Wahr, 2006). Such errors have been mitigated through the application of their destriping filter but also through the use of a number of other filters such as Gaussian (e.g., Wahr et al., 1998) and the suite of DDK filters (e.g., Kusche, 2007). Some studies (Bruinsma et al., 2010; Lemoine et al., 2007) applied constraints to the spherical harmonic coefficients so that their change in magnitude with higher degree matched some empirical pattern, thus reducing the noise in the estimated temporal gravity fields.

Rowlands et al. (2005) and Watkins et al. (2005) introduced the use of mass concentration elements (mascons) as an alternate parameterization to represent the temporal gravity field from GRACE data. A mascon is defined as a tile or region of known area on which a change in mass is estimated. They related the change in mass of each mascon (represented by a uniform thickness of water over the surface of each mascon) to spherical harmonic coefficients representing the temporal gravity field and, hence, estimated the spatial pattern of mass variations. Luthcke et al. (2006) showed that the use of mascons permitted more intuitive applications of spatial and temporal constraints in the inversion steps, resulting in temporal gravity field estimates that contained significantly less noise and did not require any further filtering. They used a regular $3^\circ \times 3^\circ$mascon geometry. Subsequent studies using mascons have adopted different approaches to defining the mascon geometry. Watkins et al. (2015) used 3° equal-area spherical caps for each mascon, while Save et al. (2016) used 1° geodesic shapes. Luthcke et al. (2013) reduced the size of their regular-shaped mascons to $1^\circ \times 1^\circ$, although they state explicitly that this is not the actual spatial resolution of the solutions, since neighboring mascons are correlated.

Different approaches have been used to improve the convergence of the inversions for temporal gravity field solutions using mascons. Luthcke et al. (2013) used empirically determined constraints on each mascon along with spatial and temporal correlations between mascons. Watkins et al. (2015) used variations derived from geophysical models (and the GRACE data itself) to regularize their solutions. Save et al. (2016) constrained their inversions using only the information contained in the GRACE measurements themselves. Their regularization matrices were time varying and did not bias their solutions toward any particular model values.

To date, all published solutions use the range rate information. Numerical differentiation of the range rate creates a range acceleration observable but amplifies short-wavelength signals while reducing the amplitude of longer-wavelength signals. The potential advantage of using the range acceleration as the primary observation (instead of the range rate) is that gravity anomaly signals caused by mass anomalies on Earth would be better localized spatially, with a spike occurring in the range acceleration observations when the satellites are approximately overhead (Save et al., 2012). However, it has not been demonstrated that the longer-wavelength signals are retained in this approach. Postfit range acceleration residuals, derived from postfit range rate residuals, have been used (Save et al., 2012, 2016) to quantify the amount of mass variation signal that was not captured by parameters when estimating the temporal gravity field. These studies did not directly use the range acceleration observations to estimate the gravity fields.

Range rate observations contain a once-per-revolution signal after passing over a disturbing mass signal. Conversely, range acceleration observations are much less affected once the satellites have passed over a mass anomaly signal. This feature can be exploited when inverting GRACE observations to estimate the spatial pattern of the temporal gravity field, provided that the long-wavelength features of the gravity field can also be sensed and estimated.

We show below that accurate mass anomalies at short and long spatial scales can be recovered from GRACE range acceleration observations, although the range acceleration observations provided in the Level-1B mission data contain a signal to noise level that precludes their use in gravity field estimation. Through an alternate numerical differentiation process, it is possible to filter out the high-frequency noise without attenuating the short-wavelength signals of the mass anomalies. The resulting temporal gravity field estimates recover accurately both the short- and long-wavelength components of the temporal gravity field.

In this paper we describe our orbit modeling and mascon parameterization used to estimate temporal gravity fields using data from the GRACE mission. We describe how the inter-satellite range acceleration data can be used to estimate the temporal gravity fields and how it reduces the typical north-south striped error pattern seen in solutions derived using the range rate. In our companion paper (Tregoning et al., 2022) we describe how we constructed our mascon field, and its effect on mitigating the smearing of signals between oceans and continents.

Table 1
Background Force Modeling Used in the Orbit Integrations

Process	Description
static gravity field	DIR-R4 (truncated to degree 200) (Bruinsma et al., 2013)
dealiasing atmosphere and non-tidal ocean	AOD1B-RL06 (Dobslaw et al., 2017)
ocean tide model	FES2014 (Carrere et al., 2015; Lyard et al., 2021)
	modified Antarctica from Padman et al. (2002)
atmospheric tides	S_1, S_2 and S_3 from the AOD1B product (Dobslaw et al., 2017)
non-gravitational accelerations	Level-1B data ACC1B/SCA1B
Cellestial body perturbation	JPL Ephemeris DE421 (Folkner et al., 2008)
Solid Earth tides	IERS 2010 non-elastic Earth (Petit & Luzum, 2010)
	including mean polar motion (Wahr et al., 2015)
General relativity	IERS 2010 standard (Petit & Luzum, 2010)

2. Methods

2.1. Orbit Modeling

We have developed the ANU GRACE processing software with which we estimate the temporal gravity field of the Earth from GRACE observations. Our software uses the classical variational approach to integrate satellite orbits (e.g., Beutler et al., 2010), then estimates adjustments to a static gravity field to quantify the "temporal gravity" field (time varying mass anomalies with respect to a mean gravity field). We parameterize the temporal gravity field using mascons and derive changes in mass on each mascon in terms of an equivalent thickness of water over the area of the mascon. We explicitly relate the change in mass of each mascon directly to the inter-satellite measurements, as described in our companion paper (Tregoning et al., 2022).

We integrate the satellite orbits using an Adams-Bashforth-Moulton 3–4 integrator. It is composed of an Adams-Bashforth (order 3) explicit step (Bashforth & Adams, 1883) as a predictor phase followed by an Adams-Moulton (order 4) step (Moulton, 1926) as a corrector phase. Table 1 describes the forces acting on the satellites in our orbit integration. Our integrator uses a 5-s step size, performs the integrations in the inertial reference frame (defined using IERS 2010 conventions, Petit & Luzum, 2010) and outputs positions, velocities and partial derivatives in the terrestrial reference frame.

We parameterize the satellite orbits using as few parameters as possible: initial position and velocity of each satellite plus one accelerometer bias and scale parameter per satellite per 24 hr period in each of the along-track, cross-track and radial directions. We iterate the orbits to converge to a set of orbital parameters that best fit the GPS positions and velocities (provided in the GNV1B data files) and inter-satellite range rate measurements (provided in the KBR1B data files) before estimating simultaneously all orbital and mascon parameters. This process is described in detail in Section 3.

2.2. Calibration of Accelerometer Observations

The observations made by the accelerometers onboard the GRACE and GRACE-FO satellites require calibration. Previous studies have differed significantly in their approach to calibrating the observations, although most studies adopt a model which includes a bias and a scale factor. The temporal estimation of bias values varies from up to 28 values per day (Rowlands et al., 2010) to daily values (e.g., Bruinsma et al., 2010; Watkins et al., 2015), while scale factor values have been estimated daily (e.g., Bruinsma et al., 2010; Rowlands et al., 2010), as monthly mean values or even fixed at a value of 1 for the radial scale factor (Watkins et al., 2015). Once the thermal control within the satellites was deactivated later in the GRACE mission (from April 2011 onwards), thermally driven non-linear variations occurred in the accelerometer measurements (Klinger & Mayer-Gurr, 2016; McGirr et al., 2021), particularly in the cross-track and radial components.

The purpose of calibrating the accelerometer observations is to turn the biased measurements into "absolute" measurements of the non-gravitational accelerations acting on each satellite. These calibrated measurements can

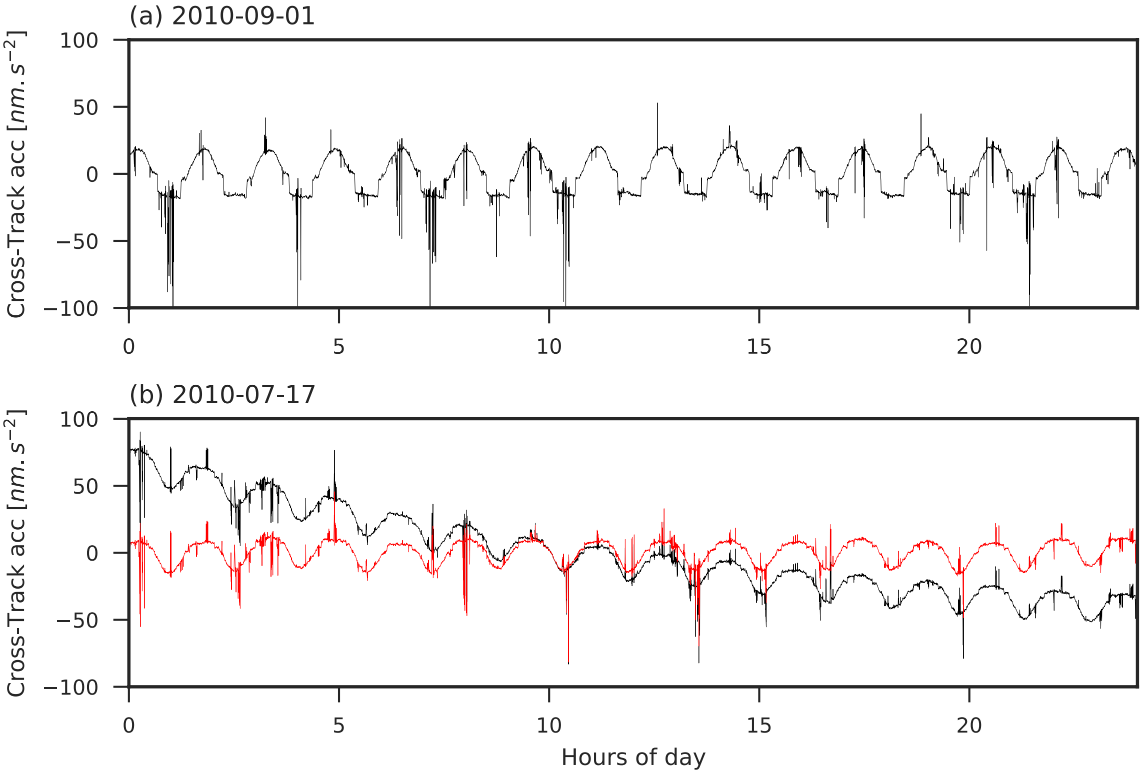

Figure 1. Uncalibrated cross-track accelerometer observations of GRACE-A for (a) a typical day (2010-09-01) when the satellites pass into the shadow of the Earth, showing the repeating pattern of the observations for each revolution. (b) 2010-07-17, including low-frequency thermal effects (black) and high-pass filtered values (red). Signals have been demeaned. The observed spikes are generated by thrust events.

then be applied directly in the integration of the satellite orbits. The measurements are a sum of the effects of atmospheric drag, solar radiation pressure, reflected energy from the Earth and linear components of the thruster firings during satellite attitude maneuvers. The atmospheric drag dominates the along-track component while the solar radiation dominates the radial component. In most cases, each of these effects has a quasi-stable signature that repeats through each orbit cycle within a single day. Therefore, one would expect that the calibrated accelerometer observations would display a repeatable pattern throughout the ∼15 orbital revolutions within a day. We find that, in general, a single bias and scale factor parameter per orthogonal axis per day is sufficient to ensure that the calibrated accelerometer observations display the expected temporal patterns in the along-track and radial directions (Figure 1a).

Thermal variations within the satellites affect the accelerometer observations and we mitigate these effects by applying a raised cosine high-pass filter as described in McGirr et al. (2021), with low- and high-edge frequencies of 0.045 and 0.055 mHz (Figure 1b). Once the low-frequency thermal effects are removed, the accelerometer observations can be calibrated using single bias and scale parameters per axis per day, as before.

2.3. Partial Derivatives

The state vector parameters ($\vec{S}_0 = (\vec{p}_0, \vec{v}_0, \vec{s}_0, \vec{b}_0)$), defining the initial condition of satellite orbits include the initial position ($\vec{p}_0$) and velocity ($\vec{v}_0$) at the start of the orbit and also the accelerometer calibration parameter scales ($\vec{s}_0$) and biases ($\vec{b}_0$). We derive partial derivatives that relate the observed positions and velocities ($\vec{o} = (\vec{p}, \vec{v})$) of a satellite to the initial state vector parameters by integrating additional orbits where each parameter is perturbed by a small amount at the start of the orbit. We calculate the partial derivative for a parameter at epoch t as the difference between the actual and perturbed orbit at each time t divided by the magnitude of the original perturbation.

$$\frac{\partial o}{\partial {S_0}^i} = \frac{\left(\vec{o}_{\delta S_0^i} - \vec{o}\right)}{\delta_{S_0^i}} \tag{1}$$

where $\vec{o}_{\delta S_0^i}$ is the instantaneous position and velocity of the satellite in the perturbed orbit, $\vec{o}$ is the instantaneous position and velocity coordinate of the satellite in the unperturbed orbit and δS_0^i is the size of the perturbation applied to the initial value of S_0 to perturb the orbit. The perturbations that we apply are 0.5 m for position parameters, 0.05 mm.s^{-1} for velocity parameters, 50 nm.s^{-2} for accelerometer bias parameters and 3% for accelerometer scale parameters. We derive partial derivatives relating our mascon parameters to the observations through an equation for the gravitational acceleration of two point sources, as described in Tregoning et al. (2022).

2.4. Prefit Residuals

The least squares inversions to solve for the mass anomaly fields use the difference (which we call here the "*prefit residuals"*) between the observations and the theoretical values computed from orbits integrated without disturbing masses. By not modeling a priori the mass anomaly fields, these prefit residuals contain the unmodelled mass anomaly signals, plus any errors in orbit modeling and/or forward models used in the orbit integration (e.g., ocean tides, non-tidal ocean and atmosphere, orientation errors for the GRACE satellites etc.). If the orbital parameter values used in the orbit integration are reasonably accurate then the prefit residuals are dominated by the effects of the unmodelled gravity field anomalies.

Typically, gravity field inversions using GRACE data have been done using the rate of change of range between the satellites, known as the *range rate*, as the observable. The time derivative of the range rate, called the *range acceleration*, also provided in the Level-1B data has not been exploited for gravity field estimation; however, range acceleration solutions have been produced (Save et al., 2019; Tregoning et al., 2017, 2018). The Level-1B range acceleration observables, $\ddot{R}_{L1B}$, provided at 5-s sampling, are generated from 10 Hz dual one-way ranges using a digital filter, where the filter is N self-Convolutions of a Rectangular time-domain window function (CRN; in this case, $N = 7$) and the time window is 70.7 s (see Case et al., 2010; Thomas, 1999 for details). The CRN filter for the range acceleration observations is actually the double time derivative of the CRN filter used to generate 5-s ranges from the same 10 Hz data. Thus, it is not the Level-1B range measurements themselves that are used to derive the 5-s range acceleration observations present in the level-1B file but the 10 Hz Level-1A dual one-way ranges. Note that all of the Level-1B range, range rate or range acceleration "observations" are, in fact, derived values, not direct observations, and no covariance or correlation information between these three observables is available in Level-1B data files.

The use of the range acceleration to estimate the temporal gravity field offers distinct advantages over the use of the range rate because it localizes the mass change signals; however, it contains high frequency noise, which needs to be removed from the Level-1B range accelerations in order to make the range acceleration a viable observable for estimating temporal gravity fields. In theory, this can be done by appropriate filtering techniques.

2.5. Derivation of Range Acceleration Data

In this section we show how we derive prefit range acceleration residuals that do not contain the high-frequency noise of the Level-1B observations. We do this through numerical differentiation of prefit range rate residuals, employing a noise robust derivative filter which helps to mitigate the high frequency noise. We show below through simulation that our range acceleration observable retains all the gravity signal but contains significantly less noise than the Level-1B range acceleration.

To derive an analytical expression from which to calculate typical range acceleration prefit residuals using simulated data, we start with the inter-satellite range, R:

$$R^2 = \vec{r}_{AB}.\vec{r}_{AB} \tag{2}$$

where $\vec{r}_{AB}$ is the vector of the inter-satellite relative position between GRACE A and GRACE B. The range rate, $\dot{R}$, is the time derivative of the range:

$$\dot{R} = \hat{e}_{AB}.\dot{\vec{r}}_{AB} \tag{3}$$

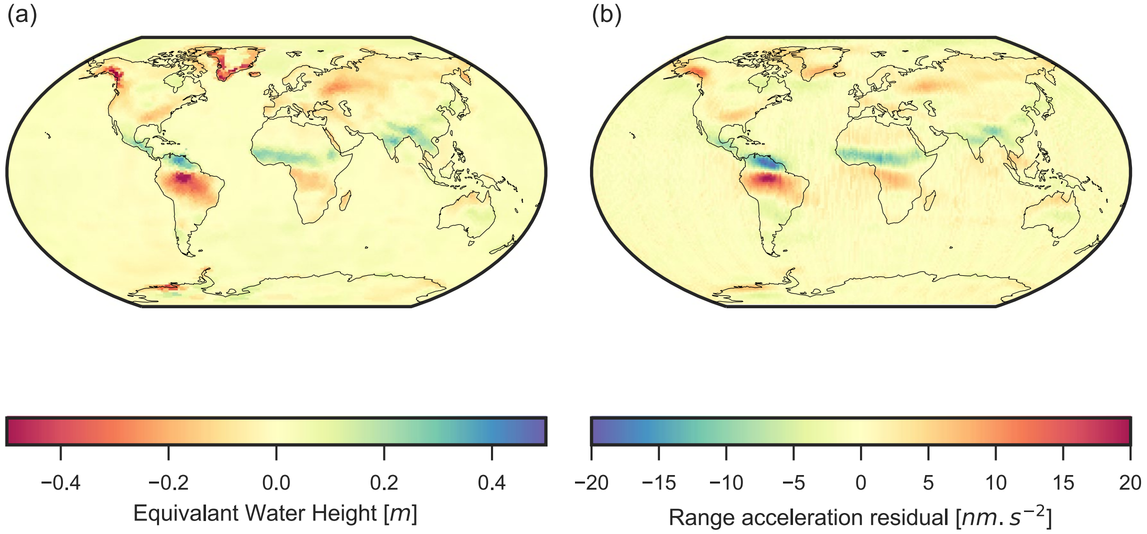

Figure 2. (a) Temporal gravity field of Luthcke et al. (2013) for September 2010, (b) Prefit Range acceleration residuals for the same month generated using Equation 7 for our "target" - "a priori" orbits.

where $\vec{\dot{r}}$ is the inter-satellite relative velocity vector and $\hat{e}$ is the unit vector of the line of sight direction between the two satellites. By differentiating Equation 3 with respect to time, one can derive an analytical expression for the range acceleration, $\ddot{R}$ (Rummel, 1979):

$$\ddot{R} = \hat{e}_{AB}.\vec{\ddot{r}}_{AB} + \dot{\hat{e}}_{AB}.\vec{\dot{r}}_{AB} \tag{4}$$

where $\vec{\ddot{r}}_{AB}$ is the inter-satellite relative acceleration vector and $\dot{\hat{e}}_{AB}$ is the time derivative of the unit vector $\hat{e}$. This has been called the "classic acceleration" approach (e.g., Rummel, 1979).

Projecting those equations in Cartesian coordinates, they become:

$$R = \sqrt{\sum \rho_i^2} \tag{5}$$

$$\dot{R} = \frac{\sum \dot{\rho}_i \rho_i}{R} \tag{6}$$

$$\ddot{R} = -\frac{\dot{R}^2}{R} + \frac{\sum \dot{\rho}_i^2 + \ddot{\rho}_i \rho_i}{R}, \tag{7}$$

where ρ, $\dot{\rho}$, $\ddot{\rho}$ are the relative difference in position, velocities and acceleration between both satellites.

2.5.1. Prefit Range Acceleration Residuals as a Temporal Gravity Field Proxy

We generated simulated GRACE orbits and extracted from our orbit integrator the positions, p, velocities, $\dot{p}$, and accelerations, $\ddot{p}$, for each satellite at each epoch in the inertial reference frame. We used these values in Equation 7 to create a set of simulated range acceleration observations. We calculated orbits for day 2010-09-01 and included in our gravity models for these orbits the temporal gravity field estimate for September 2010 of (Luthcke et al., 2013; Figure 2a) that we will call '*target*' orbits. Thus, these perturbed range acceleration observations, $\ddot{R}^t$ (where superscript t stands for target orbits) contain the effects of the temporal gravity field for this date. We also calculated the simulated range rate observable, $\dot{R}^t$ from Equation 6.

Next, we generated a second set of GRACE orbits where we did not use the temporal gravity field as part of the gravity models in the integrator (which we call our "a priori" orbits). That is, we simulated the satellites flying around just the static component of the Earth's gravity field. Once again, we extracted the positions, velocities and accelerations at each epoch for each satellite and, using Equations 6 and 7, computed the range rate and acceleration observations, $\ddot{R}^a$ (where superscript a stands for a priori orbits).

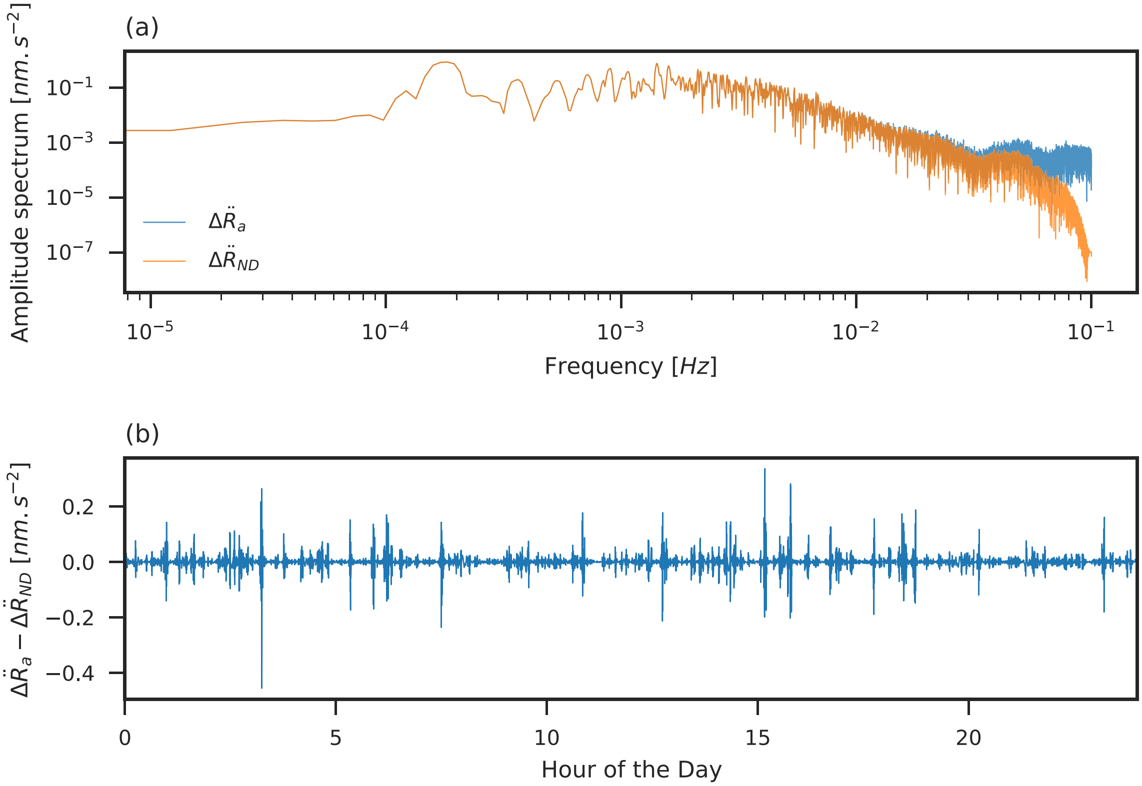

Figure 3. (a) Amplitude spectra of range acceleration residuals from a simulated temporal gravity field (Blue: values computed using Equation 7. Orange: values derived from the ND filter of the simulated range rate differences). (b) Time series for 2010-09-01 of the range acceleration difference between the analytical formula (Equation 7) and using the maximally flat derivative filter.

The difference between $\ddot{R}^t$ and $\ddot{R}^a$ provides us with simulated prefit range acceleration residuals, $\Delta\ddot{R}_a$, computed analytically and containing only the effects of the temporal gravity field on the inter-satellite observable. Plotted spatially (Figure 2b), these prefit range acceleration residuals do indeed correspond to the places on Earth where there are signals in the temporal gravity field for September 2010 (compare Figures 2a and 2b).

The amplitude spectrum of the analytically derived range acceleration residuals, $\Delta\ddot{R}_a$, are shown in Figure 3a (blue line). The gravity signal is evident at frequencies lower than 0.01 Hz, with essentially no other power present. To some extent, this is influenced by the spatial resolution with which we simulated the temporal gravity field (~200 km). Abich et al. (2019) and Tapley et al. (2019) estimated that the highest detected frequencies of the temporal gravity field were likely to be around 30 mHz, which is consistent with our simulation.

2.5.2. Range Acceleration Obtained via Numerical Differentiation of Range Rate

Mass changes on mascons will have a direct effect on the accelerations acting on the satellites. Hence we choose to use the acceleration in the range measurement to determine the gravity field, but to do this it is necessary to suppress short wavelength noise in the range acceleration prefit residuals.

We seek a means of deriving prefit range acceleration residuals using real data through numerical differentiation of the range rate data. It is important to verify that the numerical differentiation process does not contaminate or attenuate the gravity signal; therefore, we first performed the numerical differentiation (ND) on our simulated range rate observables, $\dot{R}^t$ and $\dot{R}^a$ using a maximally flat numerical differentation filter:

$$\ddot{R}_{nd} = F_{ND}\left(\dot{R}\right) \tag{8}$$

where F_{ND} is the ND filter. The derivative routine implements a 7-point maximally flat low-pass digital differentiation filter (Hosseini & Plataniotis, 2017; Selesnick, 2002) that minimizes high frequency noise in a uniform manner while producing an accurate derivative at low frequencies.

We calculated the prefit range rate residuals, $\Delta\dot{R}_a$, (being $\dot{R}^s - \dot{R}^b$), and performed the numerical differentiation on $\Delta\dot{R}_a$. This generated a second set of range accelerations, $\Delta\ddot{R}_{nd}$. Figure 3 shows the difference between the two methods on a single day (2010-09-01). Here, we found a good agreement between the derived prefit range rate residuals and those calculated analytically from simulated data, with a RMS differences of only 0.04 nm.s^{-2}. The full amplitude of the temporal gravity field is retained in the amplitude spectrum (Figure 3a, orange line) with insignificant noise having been introduced at higher frequencies and differences less than 0.4×10^{-9} m.s^{-2} in the time series (Figure 3b).

In summary, numerically differentiating prefit range rate residuals yields prefit range acceleration residuals that are insignificantly different from those generated using the analytical expression in Equation 7. Our numerical differentiation of range rate prefit residuals can substitute as a means of generating prefit range acceleration residuals. We adopt our procedure to generate prefit range acceleration residuals from real observations.

2.5.3. Prefit Range Acceleration Residuals Derived From Real Data

Range acceleration observations are provided in the Level-1B data for the microwave instrument of the GRACE mission, but they contain a very high level of noise (Tregoning et al., 2017; Figure 4a, blue curve). The difference between the Level-1B range acceleration observations and our range acceleration observations derived using Equation 7 therefore contains a higher level of high-frequency noise above 0.2 Hz. The noise is so large that it obscures the temporal gravity field signal completely in the spatial domain (Figure 4c).

To create prefit range acceleration residuals using the Level-1B data, we need to create a range acceleration observation that is not dominated by short wavelength noise. Since we do not have Level-1B observations of the cartesian accelerations required to compute the range acceleration analytically using Equation 7, we calculate the observations by differencing the observed and our computed range rates, then numerically differentiating the prefit range rate residual as described in 2.5.2 (Figure 4a, orange curve).

We applied this method to the actual GRACE Level-1B data for September 2010. That is, we difference the Level-1B range rate observations from range rates computed from our integrated a priori orbits for this day, then numerically differentiated the difference. It is perhaps not surprising that the amplitude spectrum of these prefit range acceleration residuals contains a higher level of high frequency noise (Figure 4a, orange curve) than our simulated values shown in Figure 3; however, it is clear that the part of the spectrum that contains the gravity field signal contains similar power to the simulated gravity field for this day (i.e., no signal attenuation has occurred). However, there is a significant reduction in high frequency noise compared to using the Level-1B range acceleration observable. Furthermore, the spatial pattern of signals in our range acceleration prefit residuals (Figure 4d) matches those created by simulation from the temporal gravity field estimated by Luthcke et al. (2013). This gives confidence that our prefit range acceleration residuals are both realistic and not dominated by noise.

Next, we applied a low-pass raised cosine filter to the prefit range acceleration residuals, using a cutoff frequency of 0.02 Hz. Tapley et al. (2019) showed that 0.03 Hz is the upper limit of the likely signals of the temporal gravity field, so we consider all power in the spectrum above this frequency to be noise. Applying the high-pass filter reduces this noise (Figures 4a and 4b green curve), leaving a prefit range acceleration residual that can be used with confidence in inversions for the temporal gravity field (Figure 4e). The comparison between the different maps, as well as the first 30 min of the time series (Figure 4b), demonstrates that the noise level of the range acceleration residual after this processing is at the nm.s^{-2} level.

2.5.4. Range Acceleration Observable Reduces North-South Striping in Gravity Field Solutions

The practical advantage of using the range acceleration observations, rather than the range rate observations, is that it causes a significant reduction in the presence of north-south stripes in the estimated temporal gravity fields. This occurs because there is a substantial reduction in cross-correlation between partial derivatives relating mascon parameters to the inter-satellite observations when using range acceleration rather than range rate observations.

In the inversions, the partial derivatives relating each mascon to the inter-satellite measurements are required (either range rate $\partial RR/\partial mascon_i$ or range acceleration $\partial RA/\partial mascon_i$, where i is the ith mascon number). If one calculates the cross-correlations between these partial derivatives for mascon i and all other mascons then strikingly different spatial patterns are obtained for the range rate and the range acceleration partial derivatives. To illustrate, we calculated the cross-correlations between all mascons and a single randomly selected mascon

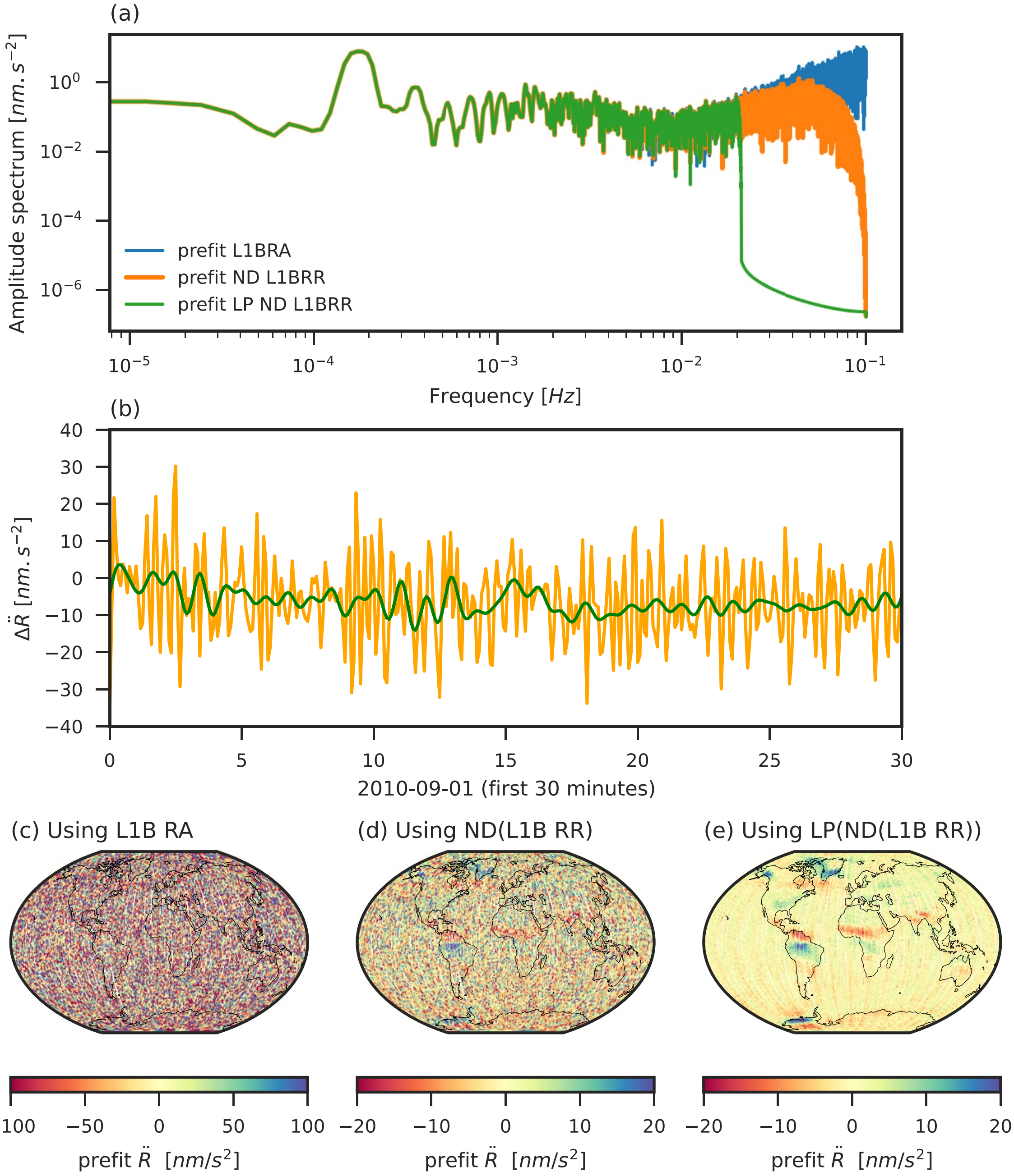

Figure 4. (a) Amplitude spectra of range acceleration residuals from GRACE data on 2010-09-01 using values computed using Level-1B range acceleration observations (blue), values derived from the numerical differentiation of the range rate prefit residuals (orange) and values derived from the numerical differentiation of the range rate residual, then low-pass filtering (green). (b) first 30 min for range-acceleration residual determined using the numerical differentiation filter (orange) and after applying the low pass filter (green). Spatial distribution of the prefit range acceleration for September 2010 using (c) Range acceleration Level-1B observations, (d) numerically differentiated prefit range rate, and (e) as for (d) but also applying a low-pass filter.

located in Panama. In the case of the range rate observations (Figure 5a), strong north-south striping is present in the cross-correlation pattern. This means that, mathematically, a change in any mascon along the flight path of the satellites passing over mascon *i* (or a change of opposite sign in mascons beside the flight path) will likely yield a very similar fit to the observations. This explains some of the north-south striping patterns that have been present in GRACE temporal gravity fields since the start of the mission. In contrast, the range acceleration partial derivatives (Figure 5b) are much more weakly correlated along track. Indeed, if anything, there is a slight

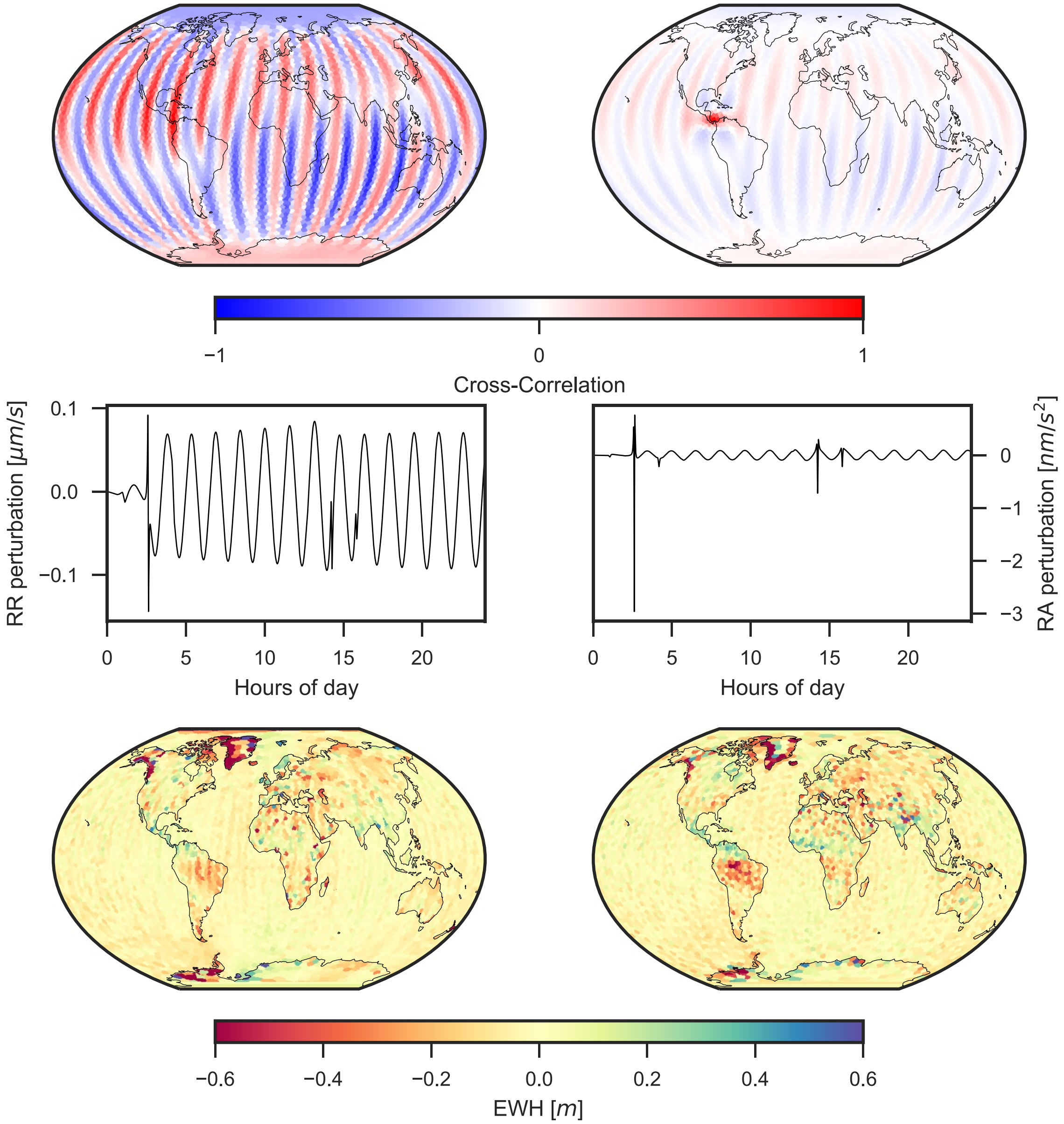

Figure 5. Cross-correlations between partial derivatives relating mascon parameters to (a) range rate observations, (b) range acceleration observations. Example time series of these partial derivatives for (c) range rate, (d) range acceleration Note the dominance in the range acceleration partial derivatives of the spike as the satellites pass over the mascon. Estimated temporal gravity fields for September 2010 using (e) range rate observations, (f) range acceleration observations. Note that the north/south striping visible in the range rate solution is significantly reduced in the range acceleration solution.

east-west cross-correlation between the partial derivatives but it is much weaker than for the north-south pattern of the range rate cross-correlations.

There is a spike in the partial derivatives of both $\partial RR/\partial mascon_i$ and $\partial RA/\partial mascon_i$ when the satellites pass close to mascon i. The high cross-correlations between range rate partial derivatives stem from the fact that the spike is $<50\%$ larger than the subsequent once-per-revolution signal induced in the partial derivatives (Figure 5c). That is, the once-per-revolution signal dominates each of the range rate partial derivative time series, which leads to high correlations (or anti-correlations) between partial derivatives of different mascons. On the other hand, the spikes in the range acceleration partial derivatives are around an order of magnitude greater than the associated once-per-revolution signals (Figure 5d), meaning that the mass change signals on the ith mascon dominate the partial derivatives and are, therefore, well located spatially. The dominance of the spike signals in the partial derivatives actually breaks the cross-correlations between partial derivatives of different mascons, as evidenced by the much smaller magnitudes of cross-correlations visible in Figure 5b.

To demonstrate the effect on a global solution, we used the temporal gravity of September 2010 from Luthcke et al. (2013) to simulate observations, then estimated the temporal gravity field using the range rate or range acceleration as the inter-satellite observable. All other analysis choices were exactly the same in the two solutions. North-South striping is evident in the range rate solution (Figure 5e) but not when using the range acceleration observable (Figure 5f). Note that we have not applied any filtering to the temporal gravity field solutions, neither spatial Gaussian filters nor any filters in the frequency domain. While we acknowledge that our range rate solution might be improved by the application of such filters, it is not the focus of this study. Furthermore a “stripe-free” solution can be achieved simply by choosing to use the range acceleration as the inter-satellite observable, without the need for any additional filtering steps.

3. Processing Workflow and Constraints

We have processed the full GRACE Level-1B data set for the period August 2002 to August 2016.

We parametrize the surface of the Earth in 12,721 mascons of about 40, 000 km^2 (roughly 200 km by 200 km, located on the ellipsoid) using the methodology of Tregoning et al. (2022). For the mascon solutions we also adopt an iterative process to refine the loads using basic linear least-squares approach (Tarantola, 2005),

$$x_j = x_{j-1} + \left(A^T C_D^{-1} A + C_M^{-1} + C_{mass}\right)^{-1} \left(A^T C_D^{-1} b\right). \tag{9}$$

where x_j are the adjustments to the a priori parameters x_{j-1} for iteration j, A is the design matrix of partial derivatives, C_D is a diagonal weight matrix of the observations, C_M is the constraint (or regularization) matrix, C_{mass} is the conservation of mass constraint and b is the vector of prefit residuals. Monthly solutions are generated by stacking the normal equations of the daily solutions, which then creates time series of mass changes on each of our mascons.

After each iteration an a priori model of the mascon loads on land is generated by computing an annual variation of the time series of each mascon, plus characterizing long-wavelength inter-annual variability as determined using a Butterworth filter with a cut-off period of 2 years. We conserve mass of the system by calculating the integrated change in mass over land and uniformly distributing any excess mass into/out of the ocean to satisfy mass conservation. The apriori model derived from iteration j is then used in iteration $j + 1$. The Jacobian matrix A for each iteration is determined by re-integrating the orbits using the mascon estimates obtained from the previous iteration as a priori values. C_D is the covariance on the observation, set to 0.07 m for the positions, 0.07×10^{-3}m.s^{-1} for the velocities, 1×10^{-9}m.s^{-2} for the range acceleration.

As shown by Save et al. (2016), it is difficult to find and apply a model covariance (C_M) that is tight enough to suppress the noise but sufficiently loose to permit the mascons to adjust to their optimal values. Figure 6 shows the impact of regularization (uniform regularization at 1m, 0.1 m and tighter variable regularization) on two monthly solution (September 2010 a-c, July 2016 d-f). Only the tight regularization is able to supress the noise in the monthly inversions and, in fact, there is still noise present in the July 2016 estimate.

We use a geographically variable C_M where different values of the uncertainties of the mascons depend on very general a priori knowledge of the hydrological processes in the region. We defined four categories of uncertainty values, 1 cm for the areas with small hydrological variations (most seas, oceans, interior Antarctica), 1.5 cm for continental mascons, 2.5 cm for the Amazon Basin and the Caspian Sea, and a 5 cm is defined for glaciated areas where large variation is expected (Greenland, Alaska, Patagonia, Antarctic Peninsula, West Antarctica; Figure 7). The C_{mass} constraint is applied to conserve the mass of the system by adding a condition that the sum of all mass adjustments is equal to zero. While these constraints are tight, as shown is the following section it is possible to estimate signal up to 8m through this process of iteration. The selection of these values is subjective and was made based on extensive assessments of noise levels in the solutions and whether we could identify any attenuation of signals by the presence of spatial coherence in the postfit range acceleration residuals. Our chosen values supress the noise in the inversions while not attenuating the signals (see Figure S1).

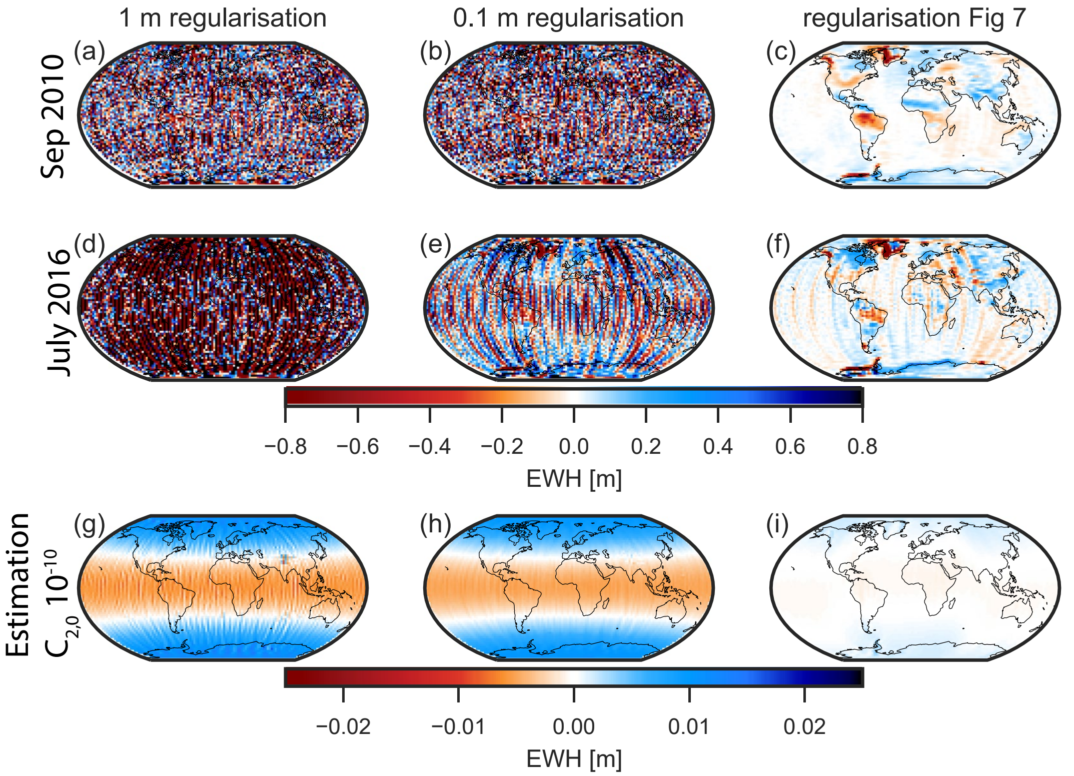

Figure 6. Effect of the regularisations Tikhonov 1 m (first column), Tikhonov 0.1 m (second column) and selected regularization (last column) for September 2010 (first row), July 2016 (second row), and its ability to recover a $C_{2,0}$ perturbation of 10^{-10}.

To assess how the regularization might affect the estimation of long-wavelength components of the gravity field, we conducted a simulation where we perturbed the $C_{2,0}$ term of the static gravity field by 1e−10, then attempted to recover the perturbation by estimating changes using the mascon parameters, using different levels of regularization. The estimated mass change fields were then converted to spherical harmonics and the estimated $C_{2,0}$

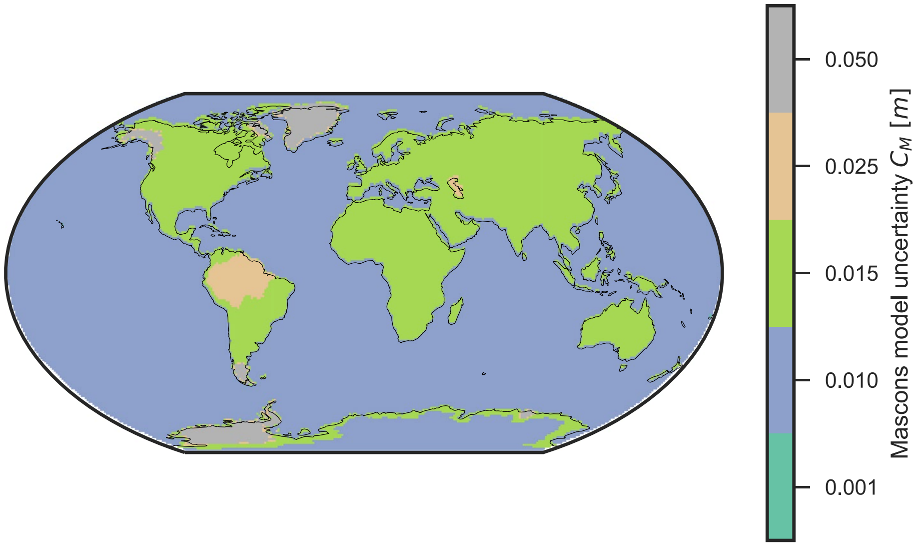

Figure 7. Covariance of the model (regularization) used for the mascons in the inversion procedure. The model used is purely diagonal (values in meters).

term compared to the perturbation. Using very loose, 1 m Tikhonov regularization we recover ~60% of the perturbation (Figure 6). However, the estimated temporal gravity field is dominated by noise using this level of regularization, indicating that stronger regularization is required. The amount of recovered $C_{2,0}$ signal decreases to ~50% if the regularization is tightened to 0.1 m (Figure 6) but the mascon estimates are still dominated by noise. When the tight, spatially variable regularization is used, we obtain our temporal gravity field estimates but $C_{2,0}$ perturbation is not well recovered at all. Thus, the estimation of $C_{2,0}$ variations from the analysis of GRACE data is strongly affected by the regularization applied to the mascon parameters.

4. Results

To validate our results, we compare our estimates of integrated water changes over specific regions with the RL06 solutions of the Center for Space Research, University of Texas at Austin (CSR; Save, 2020; Save et al., 2016) and the Goddard Space Flight Center (GSFC; Loomis et al., 2019). Differences between the three analysis approaches mean that one should not necessarily expect to find exact agreement between the solutions. The most significant differences are that (a) we use the range acceleration observable, which then requires less filtering/regularization of the results, and (b) unlike the mascons in the solutions of the other centers, our variable-shaped mascon geometry means that our mascons don't cross coastlines or the Amazon drainage boundaries (Tregoning et al., 2022). Our solution has been corrected for $C_{2,0}$ (Loomis et al., 2020), degree 1 (TN13a, Swenson et al., 2008; Sun et al., 2016), GIA (Peltier et al., 2018) and AOD1B-GAD product (Dobslaw et al., 2017). We also compare with our solution corrected only for the GIA to assess the effect of the different corrections.

4.1. $C_{2,0}$

Previous analyses of GRACE data have found significant and unrealistic noise in the estimated $C_{2,0}$ coefficients of the temporal gravity field (e.g., Watkins et al., 2015). This has led analysts to replace their estimated $C_{2,0}$ coefficients with values derived from Satelite Laser Ranging (SLR) observations (Save et al., 2016; Watkins et al., 2015). Mascon solutions have also been found to have inaccurate estimates of this long-wavelength component of the temporal gravity field, and Watkins et al. (2015) made a correction of the (implied) $C_{2,0}$ component of their mascon fields by converting to spherical harmonic coefficients, replacing the $C_{2,0}$ terms then converting back to mascons.

We converted our estimated monthly gravity fields to spherical harmonic models, then compared our $C_{2,0}$ coefficient time series with the values derived from SLR observations. Our GRACE-derived $C_{2,0}$ (Figure 8) captures the general trend of the SLR observations known as TN-11 (Cheng & Ries, 2017) and TN-14 (Loomis et al., 2020). The largest discrepancy occurs around 2006.5; converted to a spatial difference this amounts to around 5 cm of equivalent water height in the polar region. This suggests that there is a need to make a correction to our GRACE mascon solutions to remove errors in out estimated $C_{2,0}$.

4.2. Polar Ice Sheets

One of the major uses of GRACE data is in the quantification of mass loss of the polar ice sheets in Greenland and Antarctica. Our solutions for the integrated change of Greenland are in broad agreement with those of CSR and GSFC, especially in terms of annual variations (Figure 9a). Based on a least squares fit over this time period, the trends of mass loss of the different solutions are similar for the GRACE-era (2002.5–2016.5): -219.7 ± 17.4 Gt.year^{-1} for this study versus $-$ 225.7.0 $\pm$ 13.8 Gt.year^{-1} and -263.1 ± 14.8 Gt.year^{-1} for the CSR and GSFC solutions, respectively. The RMS difference between our time series and that of CSR is 852 Gt.year^{-1}, which is of similar magnitude to the difference between CSR and GSFC (700 Gt.year^{-1}). We see no significant difference between our solution with and without all the corrections ($C_{2,0}$, deg1, GAD) for the time series integrated over Greenland.

In contrast, in Antarctica (Figure 9b) we find that our solutions with and without these corrections adjustments do differ. The corrected time series exhibits a strong seasonal variations which is related to the degree 1 correction. Our integrated Antarctic mass loss signal which includes all corrections agrees broadly with the time series of CSR or GSFC (RMS = 202 Gt.year^{-1}).

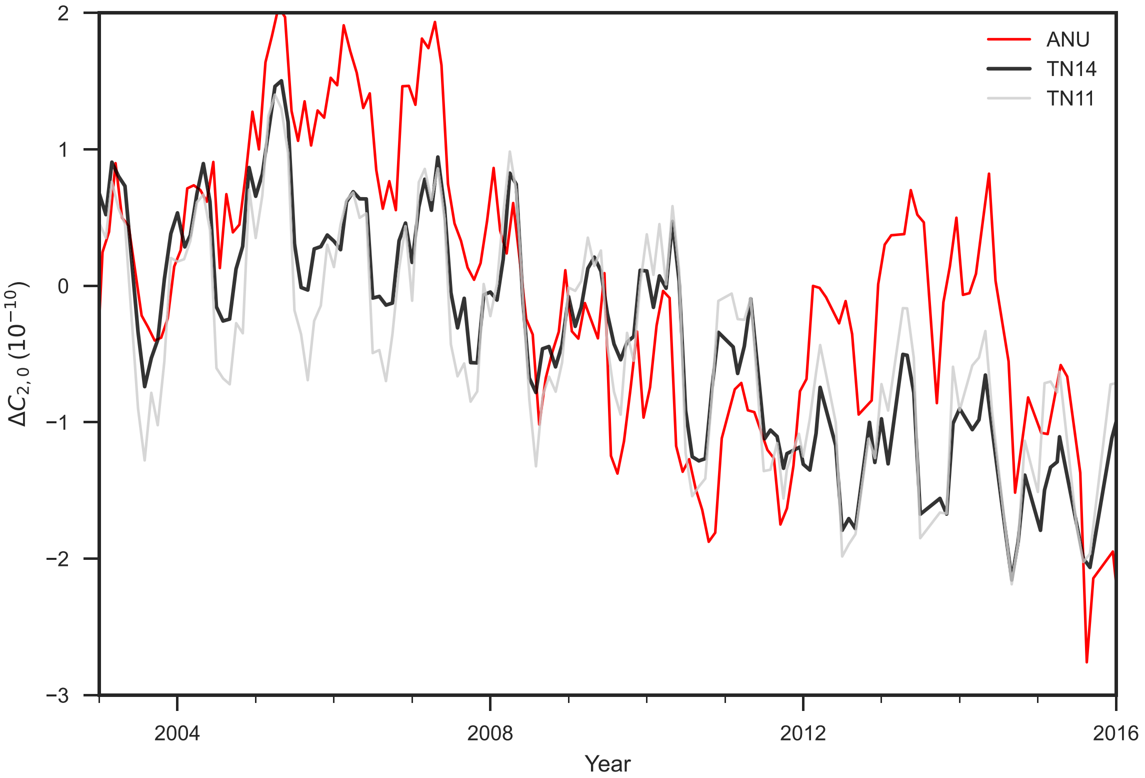

Figure 8. Comparison of the $C_{2,0}$ variation from the our GRACE solution with the SLR derived values TN11 (Cheng & Ries, 2017) and TN14 (Loomis et al., 2020) relative to their TN-14 mean value of $-4.841\,694\,573\,2 \times 10^{-4}$.

4.3. Ocean Mass Change

We summed the change in mass across all our ocean mascons and compare with the GRACE estimate of total mass change in the oceans of CSR and GSFC (Loomis et al., 2019; Save et al., 2016). Here, there is potentially a significant difference in the two approaches, since our ocean mascons essentially include the entire ocean right to the shoreline around continents, whereas those of CSR and GSFC include mascons that cross the coastline. Save et al. (2016) addressed this by breaking their mascons into smaller ocean and continent components, while Loomis et al. (2019) used a multi-iteration regularization strategy to mitigate the leakage of signal. We do not invoke any particular strategy since our mascon geometry correctly locates the signals on continent or ocean, thereby mitigating any signal leakage issue (see Figure 6 of Tregoning et al., 2022).

All time series (Figure 10) have a similar amplitude of annual variation (ANU: 12.6 ± 0.3 mm; CSR: 10.8 ± 0.3 mm; GSFC: 10.3 ± 0.2 mm) and all have a statistically significant acceleration term (ANU: 0.13 ± 0.01 mm.yr^{-2}; CSR: 0.06 ± 0.01 mm.yr^{-2}; GSFC: 0.12 ± 0.01 mm.yr^{-2}), showing broad agreement between the three solutions.

4.4. Caspian Sea and Amazon Basin

Finally, we compare two major basins which have been observed previously to have large seasonal variations as well as multi-year, non-linear trends. Here again, one might not expect a high level of agreement between our solutions and those of CSR and GSFC because our mascons are constructed to follow the shoreline of the Caspian Sea (Figure 11a) and the drainage divide of the Amazon Basin (Figure 11b), whereas the mascons of the other two centers span these natural boundaries. Our integrated time series for the Caspian Sea agrees very closely with that of CSR, whereas that of GSFC has a larger range and slightly larger annual amplitude. In contrast, our annual amplitude for the Amazon Basin (170 ± 5 mm) is about 15% smaller than those of GSFC and CSR (200 ± 4 mm and 195 ± 5 mm respectively). No significant difference is seen between any of the solutions in terms of long-term trend of total water storage change in the Amazon Basin.

(a) Greenland

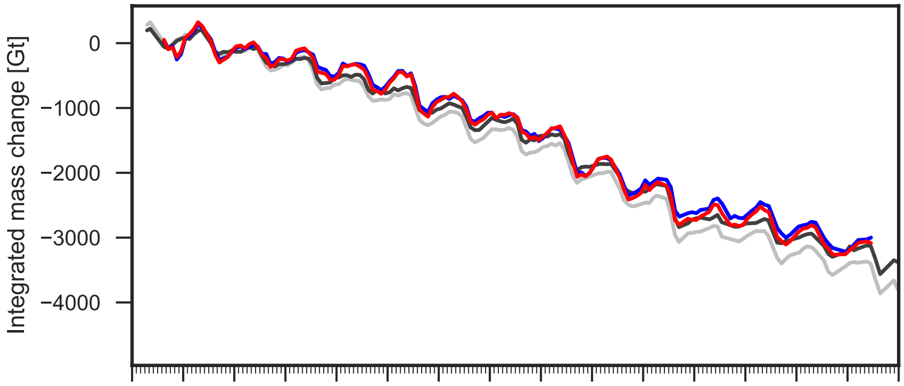

(b) Antarctica

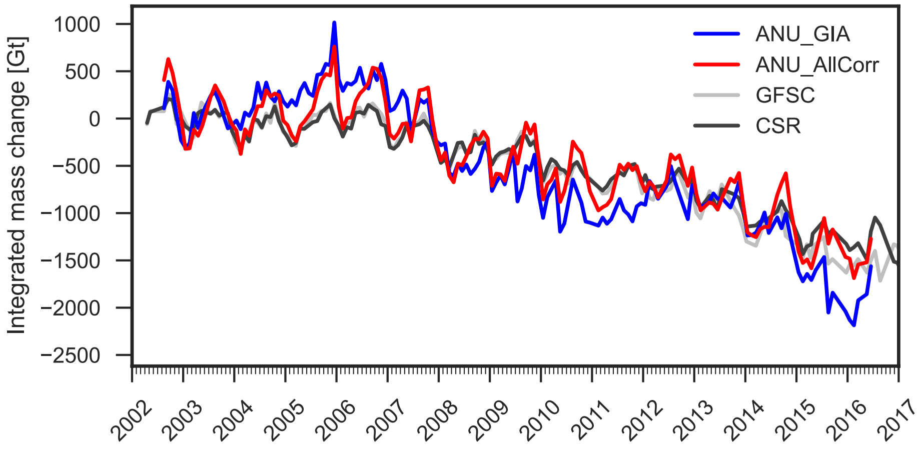

Figure 9. Comparison of the integrated mass in gigatons (Gt) over (a) Greenland and (b) Antarctica over the GRACE-era for the ANU time series in blue (our solution), the GSFC mascons solution (gray) and the CSR solution (black). All time series have been demeaned on their 2003–2004 average.

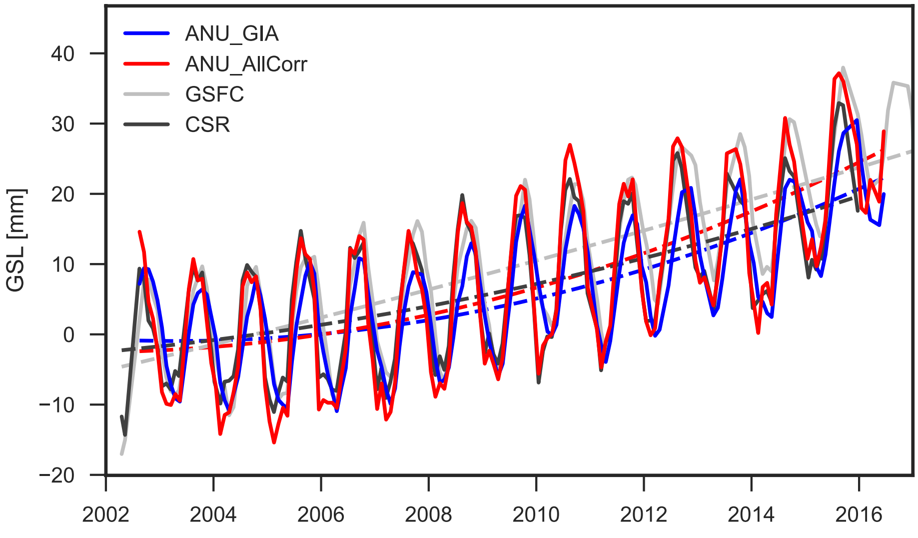

Figure 10. Comparison of the variation of the global sea level (GSL) over the GRACE-era from the ANU time series in blue (in red with correction applied), the GSFC mascons solution in gray and the CSR solution in black. All time series have been demeaned on the 2003–2004 average. The dashed lines are the second degree polynomial fits.

(a) Caspian Sea

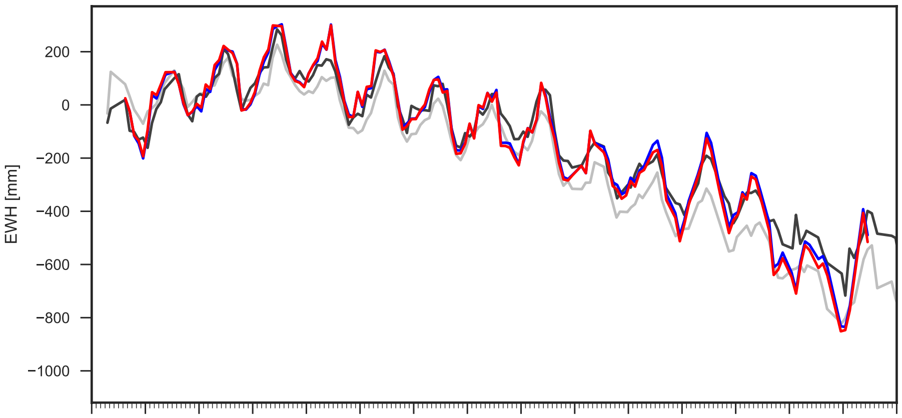

(b) Amazon Basin

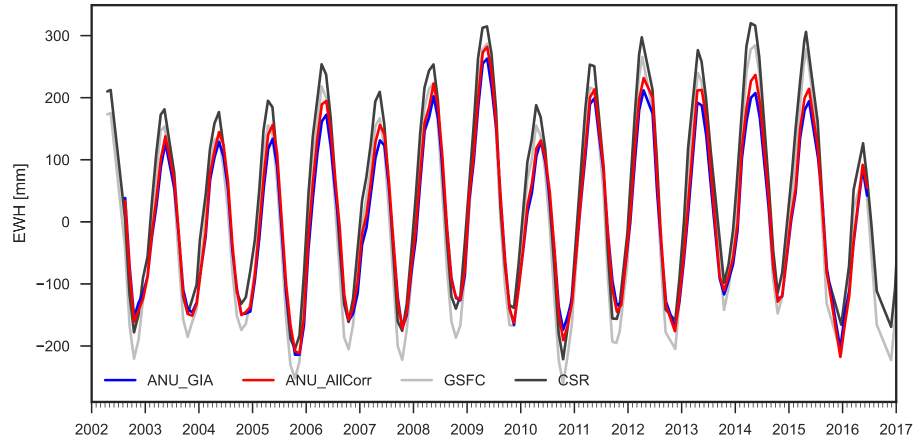

Figure 11. Comparison of the integrated mass in mm of equivalent water height over (a) ocean surface (b) the Caspian Sea and (c) the Amazonas over the GRACE-era from the ANU time series (blue, red with the $C_{2,0}$ correction), the GSFC mascons solution (gray) and the CSR solution (black). All time series have been demeaned on their 2003–2004 average.

5. Conclusions

The range acceleration observable can be used to estimate accurate temporal gravity fields from GRACE data; however, the very high levels of high-frequency noise in the Level-1B range acceleration observations cause significant errors in gravity field estimates. We reduced the noise through a combination of a maximally flat derivative filter and a low-pass filter of range rate residuals, without attenuating the gravity field signals themselves. When converted to spherical harmonics, the $C_{2,0}$ coefficients of our monthly mass anomaly fields agree broadly with the independent SLR estimates although the estimates are affected by the choice of regularization. We therefore replace the $C_{2,0}$ in our mascon solution with the TN14SLR estimate. The resulting mass anomalies compare well with other mascon estimates, both in terms of spatial pattern and temporal evolution in both continental and oceanic environments. The observed differences can be attributed to the different processing methodology and definition of the mascons geometry (cf. our companion manuscript Tregoning et al., 2022). With the successful launch of the GRACE Follow-On mission in May 2018, including a more accurate laser to measure the inter-satellite range, the use of range acceleration observations offers the potential to improve significantly the recovery of the temporal gravity field.

Data Availability Statement

Products generated from this paper and the code used to produce the result are available at https://datacommons.anu.edu.au/DataCommons/item/anudc:6133. A range of input datasets were used in this paper. The tide model (FES2014b) is available at https://www.aviso.altimetry.fr/en/data/products/auxiliary-products/global-tide-fes/

description-fes2014.html (registration required). The Level-1B GRACE data are available at https://podaac-tools.jpl.nasa.gov/drive/files/allData/grace/L1B. CSR and GSFC solutions are available respectively at http://www2.csr.utexas.edu/grace/RL06_mascons.html (Save et al., 2016; Save, 2020) and https://earth.gsfc.nasa.gov/geo/data/grace-mascons (Loomis et al., 2019). All data used for this study are freely available.

Acknowledgments
We thank Prof. B. Tapley, Dr S. Bettadpur, Dr D. Wiese and many others for fruitful discussions as we built our software and analysis capability. This research was funded in part by Australian Research Council grants DP0985080, DP130101766, DP190102382 and an Australian Space Research Program project. This project was undertaken with the assistance of resources and services from the National Computational Infrastructure (NCI), which is supported by the Australian Government. The authors thank the editor and two anonymous referees for providing thoughtful review comments which have improved this paper. Open access publishing facilitated by Australian National University, as part of the Wiley - Australian National University agreement via the Council of Australian University Librarians.

References

Abich, K., Abramovici, A., Amparan, B., Baatzsch, A., Okihiro, B. B., Barr, D. C., et al. (2019). In-orbit performance of the grace follow-on laser ranging interferometer. *Physical Review Letters*, *123*, 031101. https://doi.org/10.1103/PhysRevLett.123.031101

Bashforth, F., & Adams, J. C. (1883). *An attempt to test the theories of capillary action: By comparing the theoretical and measured forms of drops of fluid*. University Press.

Beutler, G., Jäggi, A., Mervart, L., & Meyer, U. (2010). The celestial mechanics approach: Theoretical foundations. *Journal of Geodesy*, *84*(10), 605–624. https://doi.org/10.1007/s00190-010-0401-7

Boening, C., Willis, J. K., Landerer, F. W., Nerem, R. S., & Fasullo, J. (2012). The 2011 la niña: So strong, the oceans fell. *Geophysical Research Letters*, *39*, L19602. https://doi.org/10.1029/2012gl053055

Bruinsma, S. L., Forste, C., Abrikosov, O., Marty, J.-C., Rio, M.-H., Mulet, S., & Bonvalot, S. (2013). The new ESA satellite-only gravity field model via the direct approach. *Geophysical Research Letters*, *40*(14), 3607–3612. https://doi.org/10.1002/grl.50716

Bruinsma, S. L., Lemoine, J.-M., Biancale, R., & Valès, N. (2010). Cnes/grgs 10-day gravity field models (release 2) and their evaluation. *Advances in Space Research*, *45*(4), 587–601. https://doi.org/10.1016/j.asr.2009.10.012

Carrere, L., Lyard, F., Cancet, M., & Guillot, A. (2015). FES 2014, a new tidal model on the global ocean with enhanced accuracy in shallow seas and in the Arctic region. In *EGU general assembly conference abstracts*, 5481.

Case, K., Kruizinga, G., & Wu, S. (2010). *GRACE level 1B data product user handbook*. JPL Publication D-22027.

Chambers, D. P. (2006). Evaluation of new GRACE time-variable gravity data over the ocean. *Geophysical Research Letters*, *33*(17). L027296. https://doi.org/10.1029/2006GL027296

Cheng, M., & Ries, J. (2017). The unexpected signal in grace estimates of c_{20}. *Journal of Geodesy*, *91*(8), 897–914. https://doi.org/10.1007/s00190-016-0995-5

Dobslaw, H., Bergmann-Wolf, I., Dill, R., Poropat, L., & Flechtner, F. (2017). *Product Description Document for Aod1b Release 06* (Vol. 1). GFZ German Research Centre for Geosciences Department.

Folkner, W. M., Williams, J. G., & Boggs, D. H. (2008). *The planetary and lunar ephemeris DE 421*. JPL IOM 343R-08-003. 34.

Hosseini, M. S., & Plataniotis, K. N. (2017). Derivative kernels: Numerics and applications. *IEEE Transactions on Image Processing*, *26*(10), 4596–4611. https://doi.org/10.1109/TIP.2017.2713950

Klinger, B., & Mayer-Gurr, T. (2016). The role of accelerometer data calibration within grace gravity field recovery: Results from itsg-grace2016. *Advances in Space Research*, *58*(9), 1597–1609. https://doi.org/10.1016/j.asr.2016.08.007

Kusche, J. (2007). Approximate decorrelation and non-isotropic smoothing of time-variable GRACE-type gravity field models. *Journal of Geodesy*, *81*(11), 733–749. https://doi.org/10.1007/s00190-007-0143-3

Leblanc, M. J., Tregoning, P., Ramillien, G., Tweed, S. O., & Fakes, A. (2009). Basin-scale, integrated observations of the early 21st century multiyear drought in southeast Australia. *Water Resources Research*, *45*(4). https://doi.org/10.1029/2008WR007333

Lemoine, J.-M., Bruinsma, S., Loyer, S., Biancale, R., Marty, J.-C., Perosanz, F., & Balmino, G. (2007). Temporal gravity field models inferred from GRACE data. *Advances in Space Research*, *39*(10), 1620–1629. https://doi.org/10.1016/j.asr.2007.03.062

Lo, M.-H., Famiglietti, J. S., Yeh, P. J.-F., & Syed, T. H. (2010). Improving parameter estimation and water table depth simulation in a land surface model using GRACE water storage and estimated base flow data. *Water Resources Research*, *46*(5). https://doi.org/10.1029/2009WR007855

Loomis, B., Luthcke, S., & Sabaka, T. (2019). Regularization and error characterization of grace mascons. *Journal of Geodesy*, *93*(9), 1381–1398. https://doi.org/10.1007/s00190-019-01252-y

Loomis, B., Rachlin, K., Wiese, D., Landerer, F., & Luthcke, S. (2020). Replacing grace/grace-fo with satellite laser ranging: Impacts on antarctic ice sheet mass change. *Geophysical Research Letters*, *47*. https://doi.org/10.1029/2019gl085488

Luthcke, S. B., Rowlands, D. D., Lemoine, F. G., Klosko, S. M., Chinn, D., & McCarthy, J. J. (2006). Monthly spherical harmonic gravity field solutions determined from GRACE inter-satellite range-rate data alone. *Geophysical Research Letters*, *33*, L02402. https://doi.org/10.1029/2005GL024846

Luthcke, S. B., Sabaka, T., Loomis, B., Arendt, A., McCarthy, J., & Camp, J. (2013). amp; Camp, JAntarctica, Greenland and Gulf of Alaska land-ice evolution from an iterated GRACE global mascon solution. *Journal of Glaciology*, *59*(216), 613–631. https://doi.org/10.3189/2013JoG12J147

Lyard, F. H., Allain, D. J., Cancet, M., Carrère, L., & Picot, N. (2021). Fes2014 global ocean tide atlas: Design and performance. *Ocean Science*, *17*(3), 615–649. https://doi.org/10.5194/os-17-615-2021

Martín-Español, A., Zammit-Mangion, A., Clarke, P. J., Flament, T., Helm, V., King, M. A., et al. (2016). Spatial and temporal Antarctic Ice Sheet mass trends, glacio-isostatic adjustment, and surface processes from a joint inversion of satellite altimeter, gravity, and GPS data. *Journal of Geophysical Research: Earth Surface*, *121*, 182–200. https://doi.org/10.1002/2015JF003550

McGirr, R., Tregoning, P., Allgeyer, S., McQueen, H., & Purcell, A. (2021). Reduction of GRACE accelerometer noise sources using digital signal processing methods. *Advances in Space Research*.

Moulton, F. R. (1926). *New methods in exterior ballistics*. University Chicago Press.

Padman, L., Fricker, H. A., Coleman, R., Howard, S., & Erofeeva, L. (2002). A new tide model for the Antarctic ice shelves and seas. *Annals of Glaciology*, *34*, 247–254. https://doi.org/10.3189/172756402781817752

Peltier, R., Argus, D., & Drummond, R. (2018). Comment on "an assessment of the ice-6g_c (vm5a) glacial isostatic adjustment model" by purcell et al. *Journal of Geophysical Research: Solid Earth*, *123*(2), 2019–2028. https://doi.org/10.1002/2016jb013844

Petit, G., & Luzum, B. (2010). *IERS conventions (2010) (Tech. Rep.)*. Bureau International des Poids et Mesures Sevres (France).

Riva, R. E. M., Gunter, B. C., Urban, T. J., Vermeersen, B. L. A., Lindenbergh, R. C., Helsen, M. M., et al. (2009). Glacial Isostatic Adjustment over Antarctica from combined ICESat and GRACE satellite data. *Earth and Planetary Science Letters*, *288*(3), 516–523. https://doi.org/10.1016/j.epsl.2009.10.013

Rodell, M., Famiglietti, J. S., Wiese, D. N., Reager, J., Beaudoing, H. K., Landerer, F. W., & Lo, M.-H. (2018). Emerging trends in global freshwater availability. *Nature*, *557*(7707), 651–659. https://doi.org/10.1038/s41586-018-0123-1

Rowlands, D. D., Luthcke, S., Klosko, S., Lemoine, F. G., Chinn, D., McCarthy, J., et al. (2005). Resolving mass flux at high spatial and temporal resolution using grace intersatellite measurements. *Geophysical Research Letters*, *32*. https://doi.org/10.1029/2004GL021908

Rowlands, D. D., Luthcke, S. B., McCarthy, J. J., Klosko, S. M., Chinn, D. S., Lemoine, F. G., et al. (2010). Global mass flux solutions from grace: A comparison of parameter estimation strategies-mass concentrations versus Stokes coefficients. *Journal of Geophysical Research*, *115*, B01403. https://doi.org/10.1029/2009jb006546

Rummel, R. (1979). Determination of short wavelength components of the gravity field form satellite-to-satellite tracking gradiometry: An attemp to an identification of problem aread. *Manuscript geodaetic*, *4*(2), 107–148.

Save, H. (2020). Csr grace and grace-fo rl06 mascon solutions v02. https://doi.org/10.15781/cgq9-nh24

Save, H., Bettadpur, S., & Tapley, B. D. (2012). Reducing errors in the grace gravity solutions using regularization. *Journal of Geodesy*, *86*(9), 695–711. https://doi.org/10.1007/s00190-012-0548-5

Save, H., Bettadpur, S., & Tapley, B. D. (2016). High-resolution CSR GRACE RL05 mascons. *Journal of Geophysical Research: Solid Earth*, *121*(10), 7547–7569. https://doi.org/10.1002/2016JB013007

Save, H., Poole, S., Bettadpur, S., & Nagel, P. (2019). *Grace-fo gravity solutions using variational methods with range acceleration data*. American Geophyscial Union Fall Meeting.

Selesnick, I. W. (2002). Maximally flat low-pass digital differentiator. *IEEE Transactions on Circuits and Systems II: Analog and Digital Signal Processing*, *49*(3), 219–223. https://doi.org/10.1109/TCSII.2002.1013869

Sun, Y., Riva, R., & Ditmar, P. (2016). Optimizing estimates of annual variations and trends in geocenter motion and j2 from a combination of grace data and geophysical models. *Journal of Geophysical Research: Solid Earth*, *121*, 8352–8370. https://doi.org/10.1002/2016JB013073

Swenson, S., Chambers, D., & Wahr, J. (2008). Estimating geocenter variations from a combination of grace and ocean model output. *Journal of Geophysical Research*, *113*, B08410. https://doi.org/10.1029/2007JB005338

Swenson, S., & Wahr, J. (2006). Post-processing removal of correlated errors in GRACE data. *Geophysical Research Letters*, *33*(8), L08402. https://doi.org/10.1029/2005GL025285

Tapley, B. D., Bettadpur, S., Watkins, M., & Reigber, C. (2004). The gravity recovery and climate experiment: Mission overview and early results. *Geophysical Research Letters*, *31*(9). https://doi.org/10.1029/2004gl019920

Tapley, B. D., Watkins, M. M., Flechtner, F., Reigber, C., Bettadpur, S., Rodell, M., et al. (2019). Contributions of grace to understanding climate change. *Nature Climate Change*, *9*(5), 358–369. https://doi.org/10.1038/s41558-019-0456-2

Tarantola, A. (2005). *Inverse problem theory and methods for model parameter estimation [Book]*. Society for Industrial and Applied Mathematics.

Thomas, J. B. (1999), *An Analysis of Gravity-Field Estimation Based on Inter-satellite Dual One- Way Biased Ranging*, JPL Publication 98-15.

Tregoning, P., Allgeyer, S., Herb McQueen, R. M., McClusky, S., Purcell, T., & White, H. (2018). *Estimating grace temporal gravity fields using adaptive regularisation*. Grace Science Team Meeting Postdam, 9–11.

Tregoning, P., McGirr, R., Pfeffer, J., Anthony, P., McQueen, H., Allgeyer, S., et al. (2022). ANU GRACE Data Analysis: Characteristics and benefits of using irregularly shaped mascons. *Journal of Geophysical Research: Solid Earth*. https://doi.org/10.1029/2021jb022412

Tregoning, P., Purcell, A., Allgeyer, S., McQueen, H., & McClusky, S. (2017). *The role of range acceleration observations and regularisation in the estimation of sub-monthly temporal gravity fields from grace observations*. American Geophyscial Union Fall Meeting.

Velicogna, I., & Wahr, J. (2006). Measurements of time-variable gravity show mass loss in Antarctica. *Science*, *311*(5768), 1754–1756. https://doi.org/10.1126/science.1123785

Wahr, J., Molenaar, M., & Bryan, F. (1998). Time variability of the earth's gravity field: Hydrological and oceanic effects and their possible detection using grace. *Journal of Geophysical Research*, *103*(B12), 30205–30229. https://doi.org/10.1029/98JB02844

Wahr, J., Nerem, R. S., & Bettadpur, S. V. (2015). The pole tide and its effect on GRACE time-variable gravity measurements: Implications for estimates of surface mass variations. *Journal of Geophysical Research: Solid Earth*, *120*(6), 4597–4615. https://doi.org/10.1002/2015JB011986

Watkins, M., Wiese, D., Yuan, D., Boening, C., & Landerer, F. (2015). Improved methods for observing Earth's time variable mass distribution with grace using spherical cap mascons. *Journal of Geophysical Research: Solid Earth*, *120*(4), 2648–2671. https://doi.org/10.1002/2014jb011547

Watkins, M., Yuan, D., Kuang, D., Bertiger, W., Kim, M., & Kruizinga, G. (2005). Grace harmonic and mascon solutions at JPL. In *Agu fall meeting abstracts*. (Vol. 2005, pp. G22A).